Impact of hydrogen concentration for CO_2 reduction on PdH_x

A combination study of cluster expansion and kinetics analysis

Ai, Changzhi; Chang, Jin Hyun; Tygesen, Alexander Sougaard; Vegge, Tejs; Hansen, Heine Anton

Published in:
Journal of Catalysis

Link to article, DOI:
10.1016/j.jcat.2023.115188

Publication date:
2023

Document Version
Publisher's PDF, also known as Version of record

Journal of Catalysis 428 (2023) 115188

Contents lists available at ScienceDirect

Journal of Catalysis

journal homepage: www.elsevier.com/locate/jcat

Research Article

Impact of hydrogen concentration for CO_2 reduction on PdH_x: A combination study of cluster expansion and kinetics analysis

Changzhi Ai, Jin Hyun Chang, Alexander Sougaard Tygesen, Tejs Vegge, Heine Anton Hansen *

Department of Energy Conversion and Storage, Technical University of Denmark, Anker Engelunds Vej, 2800 Kgs. Lyngby, Denmark

ARTICLE INFO

Keywords:
Active learning
Cluster expansion
CO_2 reduction
PdH_x
H concentration
Scaling relations
Kinetic activity
Selectivity

ABSTRACT

Pd hydride has shown better electrochemical CO_2 reduction reaction (CO_2RR) performance compared to metal Pd implying that H in the PdH_x surface plays a vital role in affecting the performance. Using density functional theory (DFT) calculations in combination with active learning cluster expansion and Monte Carlo simulated annealing we identify 12 stable PdH_x(111) configurations on the DFT convex hull and investigate the binding energies of intermediates in the CO_2RR and the competing hydrogen evolution reaction. Through analysis of intermediate binding energies and a microkinetic model, we identify the atomic structures of the PdH_x phase most likely to produce syngas. The high activity of the $PdH_{0.6}$ surface can be attributed to the fact that H segregation in the PdH_x(111) surface breaks the linear relation between HOCO* and CO* adsorbates.

1. Introduction

The primary driver of global climate change is carbon dioxide (CO_2) emissions in the world nowadays. It is widely recognized that it is urgent to reduce CO_2 emissions as parties to the Paris Agreement agreed "the increase in the global average temperature to well below 2 ℃ above pre-industrial levels and to pursue efforts to limit the temperature increase to below 1.5 ℃ above pre-industrial levels" [1,2]. Conversion and utilization of CO_2 is considered as a possible scheme to mitigate these emissions. Several technologies to realize the CO_2 reduction exist, such as electrocatalysis, thermocatalysis, photocatalysis, and biocatalysis. Among them, the electrochemical CO_2 reduction reaction (CO_2RR) is one of the most promising approaches for converting CO_2 to valuable fuels and chemicals [3]. In fact, the electrochemical processes of CO_2RR would involve multiple electron/proton transfer, which can generate different common products, such as 2, 6, 8, and 12 electrons for the formation of CO, CH_3OH, CH_4 and C_2H_5OH [4–6]. In general, longer reaction pathways that accompany more electron/proton transfers have lower energy conversion efficiency than shorter pathways. Converting CO_2 into the CO product only needs two electron/proton transfers during the electrochemical reaction process and thus has higher energy conversion efficiency, which shows great potential for industrial applications. However, high overpotential is generally required due to the high stability of CO_2. Under the high overpotential, the competitive hydrogen evolution reaction (HER) will also likely produce H_2. Many efforts have been made to suppress the HER, such as designing various electrocatalysts, electrodes, and so on, to promote high selectivity for the CO_2RR [7]. An alternative to finding highly selective catalysts is to tune the CO/H_2 ratio. This is because CO and H_2, the main components of syngas, can be used as downstream reactants to synthesize many basic organic chemicals and intermediates through the Fischer–Tropsch processes [8]. Therefore, it is necessary to find efficient electrocatalysts to produce syngas with a suitable CO/H_2 ratio.

The Faradaic efficiency and chemical selectivity of the CO_2RR are strongly related to the structure and chemical nature of the electrocatalysts as well as the electrolysis conditions, such as the applied potential [9]. Over the past decades, many works have been devoted to studying metal catalysts as they exhibit good catalytic activity for the CO_2RR [10,11]. Copper (Cu) is the only metal catalyst that can realize significant C–C coupling to produce multiple hydrocarbons, in addition to methane, formic acid, hydrogen, and CO [10]. Among them, up to 20% CO Faradaic efficiency can be reached at −0.85 V versus the reversible hydrogen electrode (RHE), which can be attributed to its moderate adsorption energy for carbon monoxide [10,12,13]. Gold (Au) nanoparticle electrocatalyst can exhibit a highly selective electrocatalytic reduction of CO_2 to CO, and the maximum selectivity can reach 90% Faradaic efficiency at −0.67 V vs. RHE when the size of the nanoparticle is 8 nm [14]. Furthermore, the selectivity can be higher, reaching 97% CO Faradaic efficiency toward CO at −0.52 V vs. RHE when Au nanoparticles are embedded in a matrix of butyl-3-methylimidazolium hexafluorophosphate [14]. A nanoporous silver (Ag) electrocatalyst was also reported to be able to reduce CO_2 to CO

* Corresponding author.
E-mail address: heih@dtu.dk (H.A. Hansen).

https://doi.org/10.1016/j.jcat.2023.115188
Received 26 May 2023; Received in revised form 27 October 2023; Accepted 28 October 2023
Available online 1 November 2023

with about 92% selectivity under moderate overpotentials of less than −0.5 V vs. RHE, which is 3000 times higher than its polycrystalline counterpart [15]. Non-noble metal Zinc (Zn) has recently been illustrated to be a potential alternative to Au and Ag for reducing CO_2 to CO due to its abundant reserves. A hierarchical hexagonal Zn catalyst was reported to have high selectivity up to 95% CO production at −0.95 V vs. RHE when using a CO_2-saturated 0.5 M KCl electrolyte [16]. Therefore, Cu has modest CO Faradaic efficiency and selectivity, and even though Au, Ag, and Zn selectively produce CO, they cannot generate the favorable CO/H_2 ratio with efficient CO_2RR activity [17].

Recently, metallic palladium (Pd) electrocatalyst has received attention for reducing CO_2 to CO; it not only exhibits good selectivity and activity but also can split CO and H_2 simultaneously to synthesize gas with an adjustable H_2 to CO ratios [17]. Pd is usually considered as a favorable HER catalyst, but it can also produce CO at a very similar ratio to H_2 [18]. Chen et al. revealed that carbon-supported palladium (Pd/C) nanoparticles can generate CO and H_2 simultaneously in an aqueous electrolyte with a tunable CO/H_2 ratio from 0.5 to 1, which is a favorable ratio range to perform Fischer–Tropsch reaction that already exists in the industrial processes [18]. Chen et al. continued to explore the influence of different facets of Pd with cubic and octahedral particles dominated by Pd(100) and Pd(111) surfaces, respectively [17]. Their results show that the octahedral Pd particles have better activity and selectivity than cubic Pd particles, and both can produce suitable CO/H_2 ratios between 1 and 2, which are desirable ratios for Fischer–Tropsch process. It is worth noting that experiments show that a key factor of the high performance is because Pd particles are transformed to Pd hydrides (PdH) [17,19]. In fact, there could exist different concentrations of H in Pd hydrides (PdH_x) controlled by the applied potential, which has an important influence on the CO_2RR performance [19,20]. Experiments only give the relation between the applied potential and CO_2RR performance and corresponding DFT calculations have only compared the performance of pure Pd and stoichiometric PdH. However, the best concentration of H of PdH_x surface for CO_2 reduction to CO is not given and it is unclear whether there is a saturation concentration of H.

Some previous theoretical efforts have been done to study CO_2RR or HER properties of PdH_x. Chen et al. reported the free energy diagram of Pd(111) and PdH(111). They concluded that the CO* desorption from metal Pd(111) surface could be the rate-limiting step due to strong CO* binding compared to PdH(111) [17,18]. Chorkendorff and co-workers reported hydrogen adsorption on palladium and palladium hydride at 1 bar. They showed the relation between the adsorption energy of H and surface H coverage on Pd(111) and Pd hydride slabs, and that the H binding energies became weaker as H coverage increased. They thought the adsorption and desorption of H_2 are faster on β-Pd hydride than α-Pd hydride at 1 bar [21]. Erhart et al. constructed the phase diagrams of bulk Pd hydride and Pd-Au hydride using a cluster expansion and studied their thermodynamic properties [22]. However, these theoretical efforts have not systematically investigated the effect of H concentration on CO_2RR.

This study uses an active learning cluster expansion (ALCE) model equipped with Monte Carlo simulated annealing to search for the stable composition of PdH_x(111) surfaces. Energies calculated by density functional theory (DFT) are used to train the ALCE model and find the ground state CE structures of each H concentration of PdH_x from the CE convex hull. Furthermore, we perform DFT relaxation to verify the CE convex hull and finally get the DFT convex hull to identify the ground state DFT candidates. Once the stable candidates are found, the CO_2RR activity and selectivity are further studied. As a result, PdH, $PdH_{0.97}$, and $PdH_{0.60}$ are finally screened out to be the most active candidates and able to generate CO/H_2 with suitable ratios.

2. Computational details

All spin-polarized DFT calculations are carried out to train the cluster expansion model and calculate adsorption energies using the atomic simulation environment (ASE) [23,24] and the Vienna Ab initio Simulation Package (VASP) with the projector augmented wave (PAW) method [25–27]. The Bayesian error estimation functional with van der Waals correlation (BEEF-vdW) ensemble is used for exchange and correlation functional, which performs quite well for chemisorption processes [28]. The first Brillouin zone is sampled by a $3 \times 3 \times 1$ Monkhorst-pack grid [29]. 400 eV is set for cutoff energy. The dipole correction is utilized in the z direction to remove the electrostatic dipole–dipole interaction due to periodically repeated surface slabs in all calculations. The structures are relaxed until all Hellmann–Feynman forces are less than 0.01 eV/Å and the energy convergence criterion is within 10^{-6} eV. More DFT calculation details can be found in the supporting information. All cluster expansion (CE) calculations in this work are performed with the Cluster Expansion in the Atomic Simulation Environment software package (CLEASE) developed by Chang et al. [30]. CE can greatly decrease the computational cost by mapping the first principles results onto a Hamiltonian that is fast to evaluate. The main idea of CE is to express the scalar physical quantity $q(\boldsymbol{\sigma})$ of crystal structure, which here is the electronic energy, as its configuration $\boldsymbol{\sigma}$ that is an N-dimensional vector consisting of site variables. It can be expressed as a linear expansion of cluster functions: [30,31]

$$q(\boldsymbol{\sigma}) = \mathrm{J}_0 + \sum_{\alpha} \mathrm{m}_{\alpha}\mathrm{J}_{\alpha}\phi_{\alpha} \tag{1}$$

Where J_α denotes the effective cluster interaction (ECI) per occurrence, which must be fitted. J_0 is the ECI of an empty cluster. m_α denotes the multiplicity factor illustrating the number of α per atom and correlation function ϕ is the average value of the cluster functions in cluster α. m_α and ϕ can be calculated from the crystal structure. The equation can be simplified as follows:

$$\mathbf{q} = \mathbf{X}\boldsymbol{\omega} \tag{2}$$

where $\mathbf{X}$ is the correlation functions matrix and ω is a column vector of ECI values. $\mathbf{q}$ denotes a column vector of energies here.

ECIs are fitted by the ordinary least squares method with regularization. We utilize *l1* regularization to avoid overfitting by adding a regularization term as follows:

$$\min_{\omega} \|\mathbf{X}\boldsymbol{\omega} - \mathbf{q}\|_2^2 + \lambda\|\omega\|_1 \tag{3}$$

where λ is the regularization constant and $\|\omega\|_1$ is the *l1*-norm of the column vector ω. Furthermore, 10-fold cross validation is used to evaluate the prediction performance of the model in order to improve the model reliability.

Monte Carlo simulated annealing at each H concentration of PdH_x is performed in order to search for the ground state structure of each concentration, which is carried out in CLEASE. The standard Metropolis Monte Carlo at each temperature during simulated annealing is used and has the acceptance probability $\mathcal{P}_{\mathrm{acc}}$ as follows: [30]

$$\mathcal{P}_{\mathrm{acc}} = \min\left\{1,\ \exp\left(\frac{-(E_{\mathrm{new}} - E_{\mathrm{old}})}{k_{\mathrm{B}}T}\right)\right\} \tag{4}$$

Where E_{new} and E_{old} are the energies of new and old structures, respectively. k_{B} is the Boltzmann constant and T denotes temperature. The temperatures are set as 10^{10}, 10,000, 6000, 4000, 2000, 1500, 1000, 800, 700, 600, 500, 400, 350, 300, 250, 200, 150, 100, 75, 50, 25, 2 and 1 K. For each temperature, 1000 Monte Carlo sweeps are applied (1 sweep includes N steps, where N is the number of atoms.)

The elementary reactions for CO_2RR in this work are considered as follows: [17,32]

$$\mathrm{CO_2(g)} + * + \mathrm{H^+} + \mathrm{e^-} \longleftrightarrow \mathrm{HOCO*} \tag{5}$$

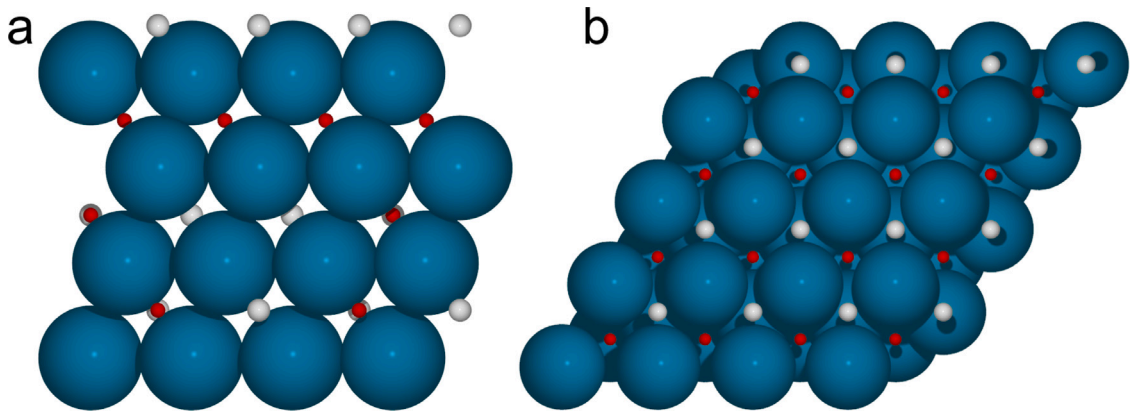

Fig. 1. (a) The side view and (b) the top view of $PdH_x(111)$ surface that take H concentration of 50% as an example. The blue spheres are Pd atoms, the white spheres represent H atoms, and the red spheres are H vacancies. (For interpretation of the references to color in this figure legend, the reader is referred to the web version of this article.)

$$HOCO* + H^+ + e^- \longleftrightarrow CO* + H_2O(l) \quad (6)$$

$$CO* \longleftrightarrow CO(g) + * \quad (7)$$

The elementary reactions for the HER can be considered by the following: [33]

$$H^+ + e^- + * \longleftrightarrow H* \quad \text{(Volmer step)} \quad (8)$$

$$H* + H^+ + e^- \longleftrightarrow H_2(g) + * \quad \text{(Heyrovsky step)} \quad (9)$$

A kinetic model is applied to analyze the activity for the CO_2 reduction to CO. The net reaction rates of three elementary reactions are illustrated as: [32,34]

$$r_1 = k_1\theta_* p_{CO_2} - \frac{k_1}{K_1}\theta_{HOCO*} \quad (10)$$

$$r_2 = k_2\theta_{HOCO*} - \frac{k_2}{K_2}\theta_{CO*} \quad (11)$$

$$r_3 = k_3\theta_{CO*} - \frac{k_3}{K_3}\theta_* p_{CO} \quad (12)$$

where k_1, k_2, k_3 denote forward rate constants of the three elementary reactions for CO_2RR. K_1, K_2, K_3 represent the corresponding equilibrium constants. p and θ represent the corresponding partial pressure and surface coverage, respectively. Experimental vapor pressures are utilized for them in this work. The partial pressure of H_2O is 3534 Pa and CO partial pressure is 5562 Pa [35]. The partial pressure of both CO_2 and H_2 are under standard pressure 101,325 Pa [10,35]. Further details for the calculations for Gibbs free energy and the kinetic model can be found in our previous work and the supporting information [34].

3. Results and discussion

To illustrate the structures of the $PdH_x(111)$ surface, we take an H concentration of 50% as an example here and display the side and top views in Fig. 1. The structure has four bilayers, including 16 Pd atoms and up to 16 H atoms. It can be seen that PdH_x has a Pd atom (blue spheres) framework, with the smaller H atoms (white spheres) filling octahedral sites between the larger Pd atoms. Red virtual atoms show H vacancies. The $PdH_x(111)$ slab is cut from the optimized bulk PdH with the crystal constants $a = b = c = 4.138$ Å and the slab size is $4\times4\times4$ with $a = b = 11.704$ and $c = 28.362$ Å. Here, we ignore the crystal constants variation when the H concentrations change because they vary only in a small range, approximately 0.2 Å from 0 to 1 for H concentration, which is less than 5% of the lattice constants of PdH [36]. Besides, previous work reported the strain of PdH only has a small impact on the performance of CO_2RR and HER [37]. There can be up to 64 H atoms in the $PdH_x(111)$ surface as shown in Fig. 1. It is impossible to run DFT calculations for all the possible structures (2^{64} neglecting symmetry). Instead, we utilize an ALCE surrogate method. The workflow of the ALCE for $PdH_x(111)$ is shown in Figure S1. After defining the CE settings, we generate 50 random H concentration structures of PdH_x to form the initial database pool and then relax the structures to get their DFT energies, which can be used to train the CE model and get the initial ECI values. If the root mean square error (RMSE) between DFT energies and CE energies is less than 5 meV/atom, we consider the CE model converged. Otherwise, more random structures will be generated and run by DFT, which are finally added to the database pool to verify if the CE model is converged. Once we have the converged the CE model, Monte Carlo simulated annealing (MCSA) with the CE calculator is performed to search for ground state structures for each H concentration of PdH_x, which gives 63 MCSA in total because the numbers of H range from 0 to 64 (concentration from 0 to 1) except pure slabs Pd(111) and PdH(111). The CE convex hull can be calculated according to all ground state structures at each concentration of H of PdH_x. Theoretically, the stable structures could be found from the vertices of the CE convex hull at this point. However, considering the uncertainty of the processes, the obtained ground state structures should be verified by DFT calculations. Therefore, the possible stable candidates of the CE convex hull are further collected, relaxed by DFT calculations, and finally added to the database pool to continue the next new round. At the same time, the DFT convex hull is also carried out until its convergence. The criterion of convergence is defined that the shape of the DFT convex hull will not change for three rounds. After that, the final stable candidates can be found according to converged DFT convex hull and their CO_2RR activity and selectivity toward CO and H_2 are further studied.

To study stable compositions of $PdH_x(111)$, CE calculations are performed using the CLEASE package. Fig. 2a shows the linear fit between CE energies (E_{CE}) and DFT energies (E_{DFT}) when we have 50 random structures in round 1. It can be seen that both 10-fold cross validation error and RMSE are really small, 1.043 meV/atom and 0.450 meV/atom, respectively, which illustrates that the CE model is really good for the $PdH_x(111)$ surface. The ECI value distribution as a function of cluster diameter (1st, 2nd, 3rd, or 4th nearest neighbor) is displayed in Fig. 2b. It can be noticed that the ECIs of 0, 1, and 2-bodies are larger, while there are more 3-body and 4-body ECI values closer to 0. To avoid overfitting, we choose to use up to 4-body interactions and neglect high terms. To get accurate stable compositions, ALCE is carried out to deal with the uncertainty of the CE. After 9 rounds, the DFT convex hull is converged, which means the vertices of the DFT convex hull are unchanged in the last three rounds as shown in Figure S6 and Figure S7. It should be mentioned that most stable structures can be

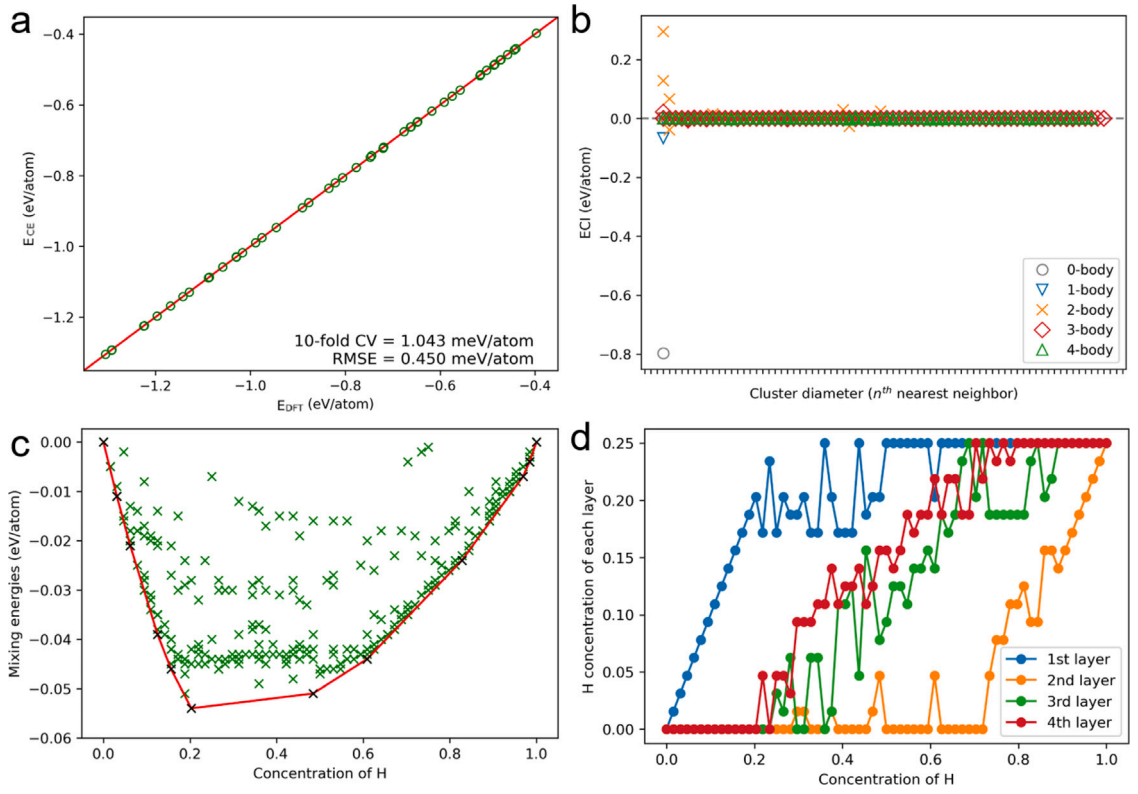

Fig. 2. (a) The linear fit of E_{CE} and E_{DFT} for 50 random structures. (b) The ECIs distribution obtained from cluster expansion fitting. (c) The DFT convex hull curve of mixing energy as a function of H concentration in round 9. (d) The H concentration of each layer as a function of the total concentration of H for the structures of the DFT lowest energies in each concentration.

found in the early rounds, which can be observed in round 2 in Figure S6b, and only a small part of more stable structures are further found in the rest of rounds until round 7. In addition, the fitting RMSEs remain small during the 9 rounds as displayed in Figure S4 and Figure S5, meaning that the CE models remain good. For each round, simulated annealing at each H concentration is calculated to find ground state structures as the example round 1 in Figure S3. As shown in Fig. 2c, 12 stable candidates can be finally obtained and are marked by black crosses. They are Pd_{64}, $Pd_{64}H_2$, $Pd_{64}H_4$, $Pd_{64}H_8$, $Pd_{64}H_{10}$, $Pd_{64}H_{13}$, $Pd_{64}H_{31}$, $Pd_{64}H_{39}$, $Pd_{64}H_{53}$, $Pd_{64}H_{62}$, $Pd_{64}H_{63}$ and $Pd_{64}H_{64}$ and the corresponding H concentrations are 0, 0.0313, 0.0625, 0.1250, 0.1563, 0.2031, 0.4844, 0.6094, 0.8281, 0.9688, 0.9844 and 1, respectively. The side and the top view of optimized example structures among them can be found in Figure S10. Fig. 2d shows the H distributions of each layer as a function of total concentrations of H in the slabs for the slabs of the DFT lowest energies in each concentration. The first layer is first filled up with H, then the fourth and third layers are filled up, respectively. Finally, the sublayer (second layer) will be finally filled at last. Possible artifacts due to the finite thickness of the model slab should be considered. To further confirm our conclusion, the $PdH_x(111)$ structures with more atomic layers with one missing layer are explored as displayed in Figure S11 and S12 in the supporting information. It can still be found that removing the sublayer H has the lowest energy and thus will be filled at last, independent of the slab thickness. In addition, semi-grand canonical Monte Carlo calculations are implemented to study H chemical potential, temperature, and pressure influence on H concentration as shown in Figure S14, S15 and S16 and the corresponding analysis can be found in the supporting information. Besides, all bare candidates surfaces are used to study the Pourbaix diagram and the phase transformation process from Pd to PdH under the applied potential in Fig. 5c–d assuming the surface to be in equilibrium with protons and electrons at all potentials. The corresponding computational details can be found in the supporting information. Fig. 5c shows the relative free energy of surface structure as a function of potential at pH 7.3, where the H concentration increases when the larger potentials are applied. The corresponding H concentration as a function of applied potential is shown in Fig. 5d. This displays metal Pd can be completely transformed to Pd hydride at a potential of about −0.6 V vs. RHE assuming the surface is in equilibrium with protons and electrons. However, characterization of Pd aerogels by Schmidt and co-workers suggests H concentration is saturated around 60% already at −0.1 V, [20] which suggests the surface can be in equilibrium with H_2 gas rather than protons and electrons. In that case, the $Pd_{64}H_{39}$ surface is likely the active surface for CO production.

After identifying stable candidates on the DFT convex hull, their CO_2RR and HER performances are further studied. Fig. 3a shows the different adsorption sites of a random structure, which are displayed in small green spheres. They are automatically found according to local similarity, which compares the similarity of local structure as displayed in Fig. 3c. The similarity is defined by comparing the neighbor list information of each adsorbate within a 2.8 Å cutoff sphere, including numbers of neighbor atoms, neighbor element types, and distance lists between adsorbate and neighbor atoms. We consider they are the same adsorption site if the similarity is 1; otherwise, they are different sites. Here only the top site, fcc site, and hcp site are considered, and the fcc sites very close to H atoms (less than 1 Å) are not considered because adsorbates located in these sites can easily react with the neighboring H. We do not consider bridge sites because they are unstable. All information on surface structures with adsorbates on all unique sites can be found in our database [38]. Binding energies of adsorbates of HOCO*, CO*, OH* and H* on the most stable sites of all PdH_x candidates are shown in Fig. 3b and the corresponding data can be found in Table S3. It can be seen that the binding energies of all adsorbates gradually increase as the concentration of H goes up from 0 to 1, especially for the adsorbate CO*. The CO_2RR free energy diagram of all candidates with adsorbates on the most stable sites is displayed

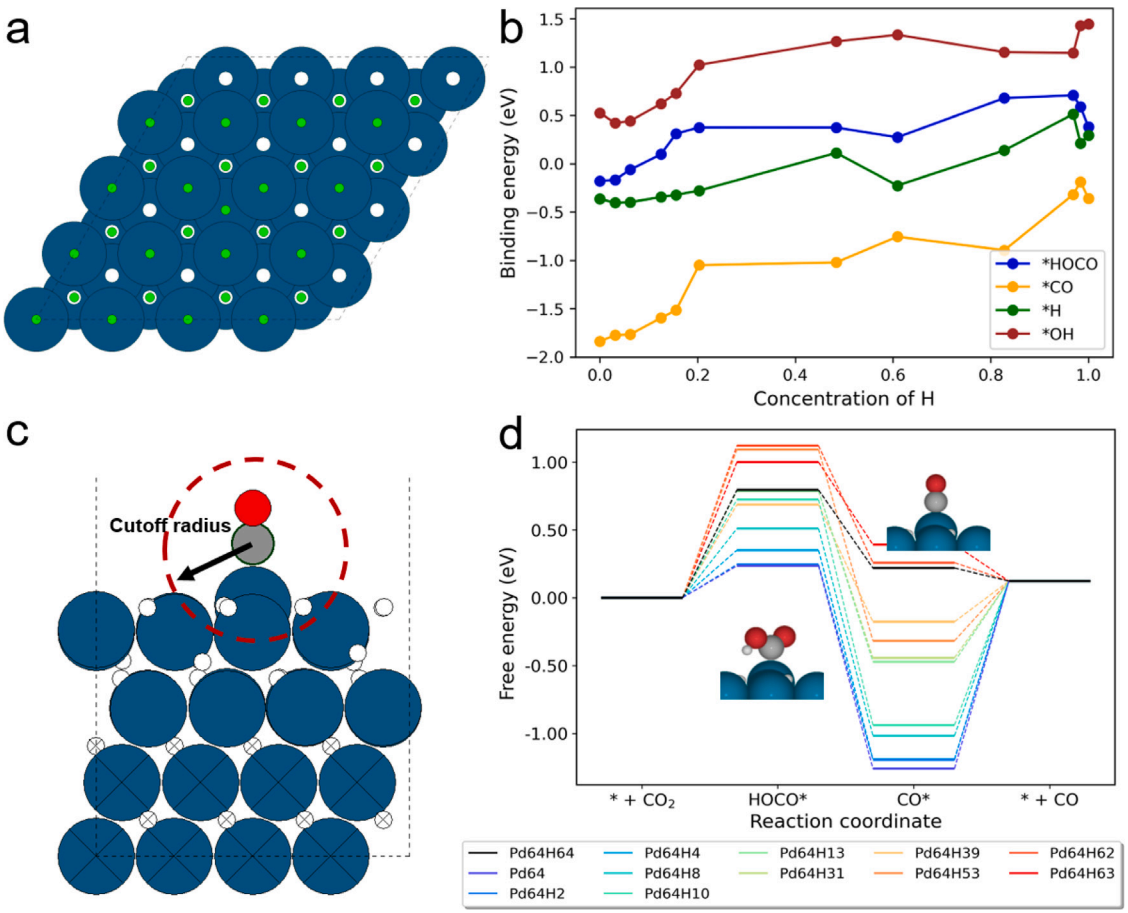

Fig. 3. (a) Adsorption sites schematic diagram on $PdH_x(111)$ surface. (b) Binding energies of HOCO*, CO*, OH*, and H* as a function of H concentration. (c) Cutoff sphere schematic diagram of adsorbate on $PdH_x(111)$ surface. (d) Free energy diagram of CO_2RR of candidates. The insets show HOCO* and CO* adsorption surface structures. The blue spheres are Pd atoms, the small white spheres represent H atoms, the grey spheres are C atoms, the red spheres are O atoms and the small green spheres denote adsorption sites. (For interpretation of the references to color in this figure legend, the reader is referred to the web version of this article.)

in Fig. 3d, and the corresponding data can be found in Table S4. We notice that most surfaces have very negative binding energies and thus have strong CO* binding, which results in CO* poisoning, especially for candidates with low H concentration. For example, the free energies of Pd_{64}, $Pd_{64}H_2$, $Pd_{64}H_4$, $Pd_{64}H_8$ and $Pd_{64}H_{10}$ at CO* step are −1.259, −1.196, −1.189, −1.017 and −0.938 eV, respectively. They have so strong CO* binding that CO* is very hard to release from the surface, which is the reason why CO* poisoning happens. This can also be found in Figure S13e. On the other hand, for candidates with high H concentration, their free energies at HOCO* are very high. For example, the free energy of $Pd_{64}H_{62}$ at the HOCO* step is 1.121 eV, which is too weak to bind HOCO* at low overpotential. Therefore, the ideal CO_2RR candidate should have strong HOCO* binding and weak CO* binding. It is worth noting the PdH surface with full H occupation does not have too high HOCO* free energy step (0.79 eV), and weak CO* free energy (0.22 eV) and thus no CO* poisoning. Besides, $Pd_{64}H_{63}$ has very weak CO* binding, 0.392 eV of CO* free energy, and acceptable HOCO* free energy. $Pd_{64}H_{39}$ has weak HOCO* binding free energy (0.686 eV) and acceptable CO* adsorption. Thus, $Pd_{64}H_{64}$, $Pd_{64}H_{63}$ and $Pd_{64}H_{39}$ are possible candidates of CO_2RR, which is consistent with the activity volcano in Fig. 5a.

To further understand the catalytic performance of $PdH_x(111)$ surfaces, the scaling relations between different adsorbates are shown in Fig. 4 and the binding energy relations with error ellipsoids can be found in Figure S13. The relations E_{CO*} vs. E_{HOCO*}, E_{OH*} vs. E_{HOCO*}, E_{H*} vs. E_{HOCO*}, E_{OH*} vs. E_{CO*}, E_{H*} vs. E_{CO*} and E_{H*} vs. E_{OH*} are displayed in 4a–f, respectively, and their R^2 values are given, which is a statistical measure to illustrate how well the linear scaling relations are fitted. For the ideal scaling relation, the R^2 value is close to 1. Otherwise, it is worse if the R^2 value is close to 0. We can see that their R^2 values are 0.72, 0.65, 0.68, 0.87, 0.77, and 0.60, respectively, which demonstrates that they have good scaling relations. However, it can also be noticed that there are some obvious outliers. For example, $Pd_{64}H_{39}$ and $Pd_{64}H_{53}$ in Fig. 4a are far from the best-fit line. This might be attributed to H segregation or/and an electronic effect as shown in Figures S8, S9, S20, and S22, which breaks the scaling relation. For both surfaces above, the H concentration distributions of the slab without adsorbates and the slab with CO* show that there is H segregation, where a small part of H atoms in the first layer moves into the second layer for the slab with CO* as displayed in Figure S8 and S22b. It is, however, difficult to precisely quantify how the H distribution affects the binding of reaction intermediates as multiple geometric variations are present between slabs with different H concentrations and adsorbates. Considering the electronic effect, the d-band center for $Pd_{64}H_{39}$ with CO* slightly increases, while d-band center for $Pd_{64}H_{53}$ with CO* slightly increases compared to clean slab as displayed in Figure S18, and S22a. This is consistent with the weak CO* binding on $Pd_{64}H_{39}$, and strong binding on $Pd_{64}H_{53}$.

A kinetic model explores the CO_2RR activity for the $PdH_x(111)$ surfaces. Fig. 5a shows the activity volcano at −0.5 V overpotential at room temperature. The current density depends on both E_{HOCO*} and E_{CO*}, which is more accurate than a single descriptor. We notice that PdH_x with low H concentration is far away from the apex of the volcano due to the strong CO binding, which means they have poor kinetic activity. The completely H-filled $Pd_{64}H_{64}$ is the closest to the apex, illustrating that it has the best activity. In addition, $Pd_{64}H_{39}$ and

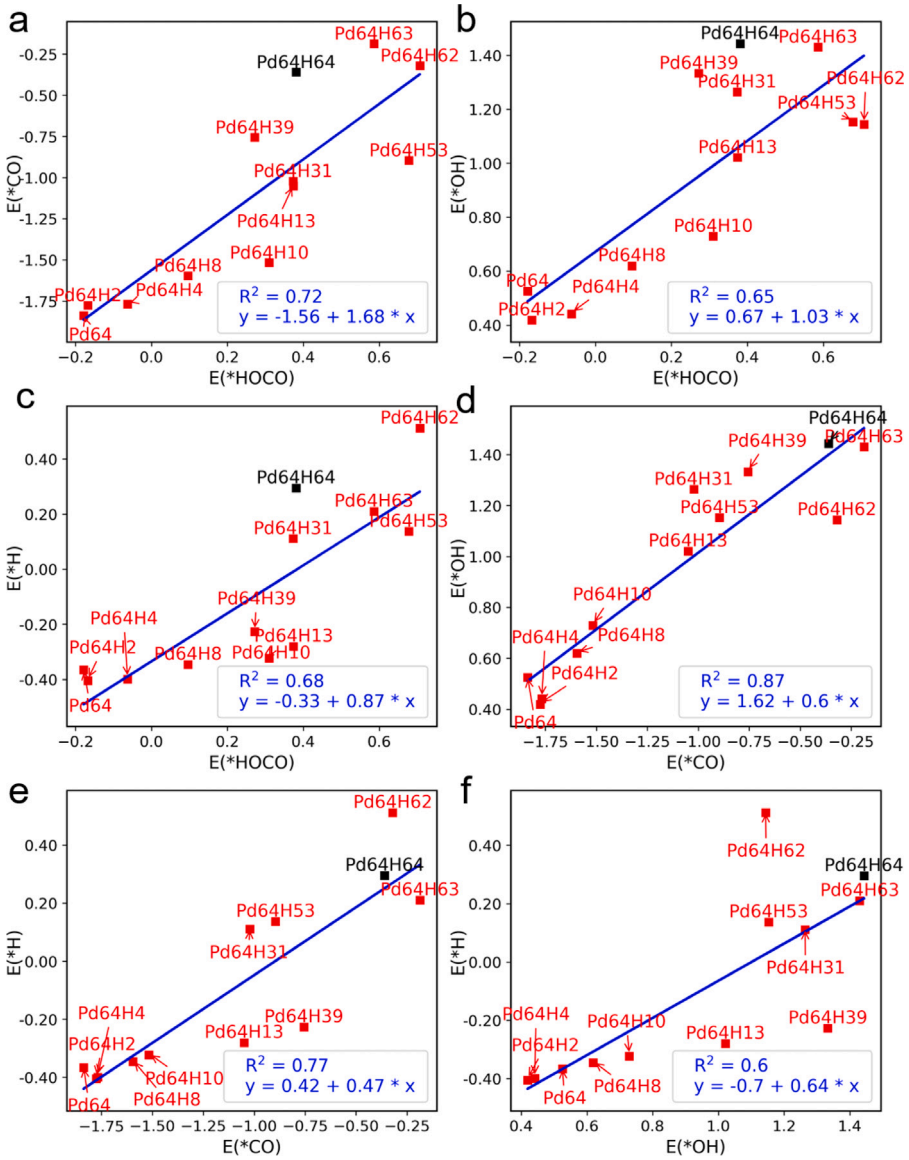

Fig. 4. Scaling relations for adsorbates on PdH_x(111) configurations on the convex hull.

$Pd_{64}H_{63}$ also exhibit good kinetic activity for higher H concentration. In order to consider the effect of the lattice constant on the activity, the HOCO* and CO* binding energies of $Pd_{64}H_{39}$ are studied as an example. The lattice constant change of bulk PdH_x can be seen in Figure S23, and the lattice constant of bulk $Pd_{64}H_{39}$ is approximately 98.3% of bulk $Pd_{64}H_{64}$. After calculating the binding energies of the $Pd_{64}H_{39}$ surface with 98.3% lattice constant, we find that both HOCO* and CO* binding energies are slightly weaker than on $Pd_{64}H_{39}$ without considering the variable lattice constant (from 0.272 to 0.324 eV for HOCO*, and from −0.756 to −0.659 eV for CO*). This is well consistent with the previous paper [37]. Therefore, $Pd_{64}H_{39}$ is more active (87.6% improvement) for the CO_2RR when the lattice constant is allowed to vary. Besides, according to Fig. 4b, we can see that the OH* binding energies on $Pd_{64}H_{64}$, $Pd_{64}H_{39}$ and $Pd_{64}H_{63}$ are weak, so OH* will not poison them. Fig. 5b shows the selectivity of all candidates toward CO and H_2. We compare the binding energies of the first step of the CO_2RR and the HER. If the binding energy of H* is lower than that of HOCO*, it means HER is thermodynamically preferred over CO_2RR and the catalyst tends to produce more H_2. We notice that all of the candidates tend to generate more H_2 as shown in Fig. 5b. Besides, $Pd_{64}H_{64}$ is very close to the black dashed line and can produce more CO, and thus its CO/H_2 ratio is closer to components of syngas compared to other candidates.

The statistical distribution of all candidates is calculated to reveal the effect of H and Pd on binding energies. Here, the statistical data of binding energies includes all possible adsorption sites on all the candidate surfaces. Fig. 6a-d display the frequencies of H, Pd, and the total atoms within a sphere with a 2.8 Å radius centered on the adsorbate as a function of the binding energies of HOCO*, CO*, H* and OH*, respectively. In addition, Fig. 6a–b indicate the most favorable binding energy for HOCO* and CO* marked in blue, respectively. We see the tendency that the binding energies for all adsorbates are weaker when there are H atoms within the cutoff sphere of adsorbates. The fitted Gaussian distributions of H are also shown in the yellow curves in Fig. 6. Their positions at the center of the peak are 0.60, −0.15, 0.44, and 1.52 eV, respectively, which are relatively weak in their corresponding binding energy distributions. Therefore, it can be concluded that H atoms weaken the binding energies of all adsorbates on PdH_x surface. To further verify the conclusion, the partial density of states (PDOS) of the d-band is calculated. Figure S17 shows the PDOS of the bare surfaces of all candidates, and the corresponding d-band centers are given. It can be seen that d-band centers gradually

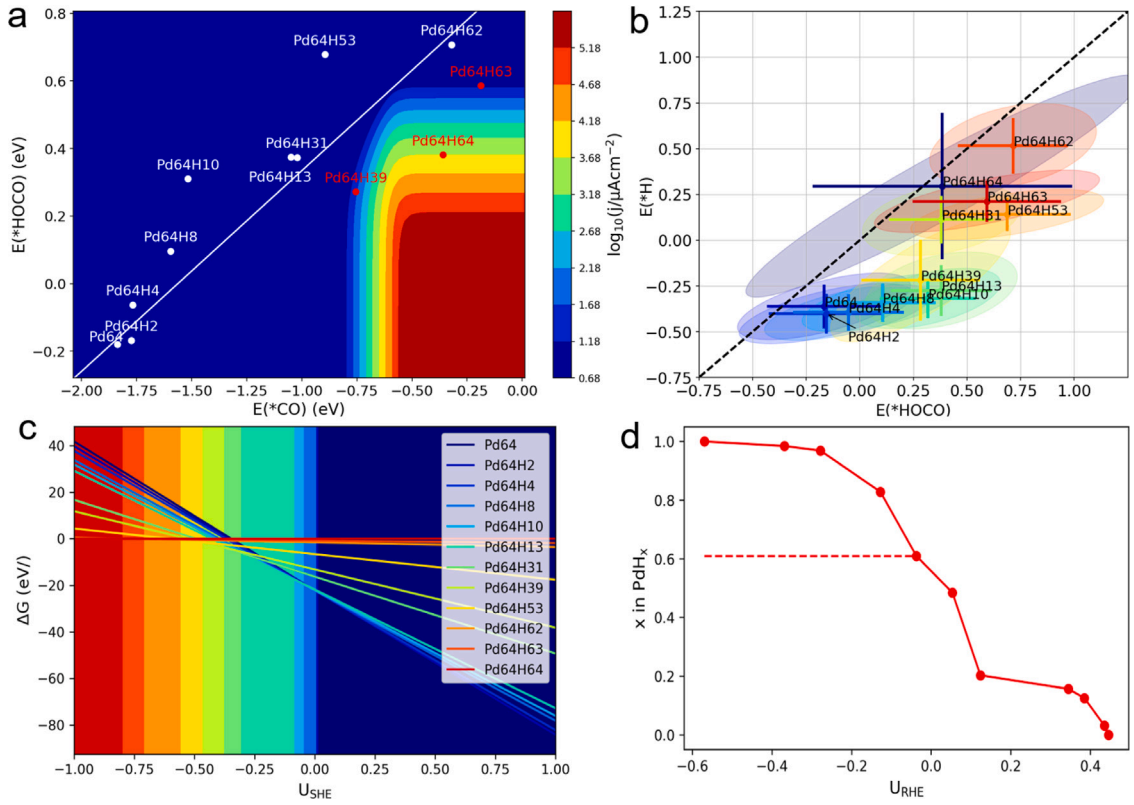

Fig. 5. (a) Activity volcano plot of PdH_x(111) candidates for CO_2RR at −0.5 V overpotential. (b) Selectivity plot toward CO and H_2. (c) Stability of ground state structures at pH 7.3. (d) The concentration of H as a function of potentials. The dashed line shows the saturation of H if the surface is in equilibrium with H_2 at 1 bar.

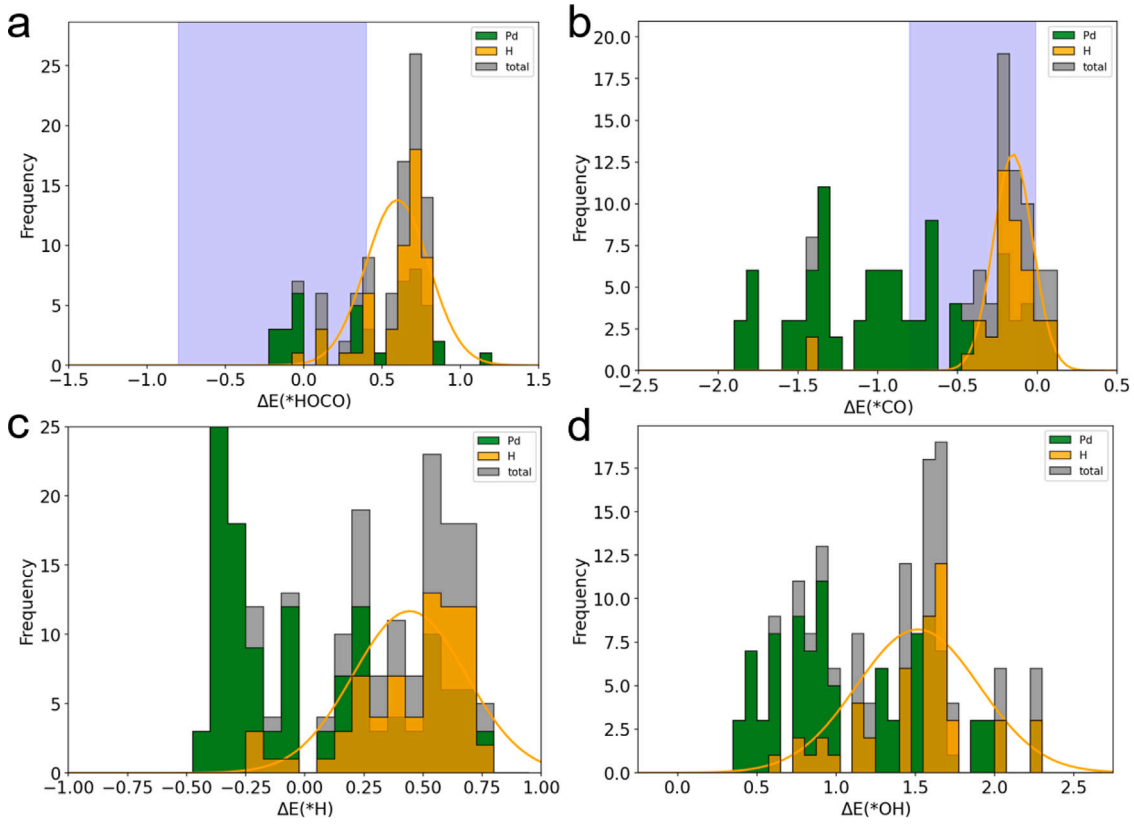

Fig. 6. Distribution of atom Pd and H of all candidates within the cutoff sphere as a function of HOCO*, CO*, OH*, and H* binding energies. The yellow curves are fitted Gaussian distribution of H. (For interpretation of the references to color in this figure legend, the reader is referred to the web version of this article.)

decrease as H concentrations increase. The linear fit between d-band centers and H concentrations is also shown in Figure S18. The R-squared value is used to describe the degree of their linear relation. The linear relation will be stronger if the R-squared value is closer to 1. The R-squared value is 0.87 in Figure S18 and thus they have strong linear relation. The lower d-band center means weaker binding energy [39]. We further calculate d-band centers for surfaces with HOCO* and CO* to support this. Figure S19 and Figure S22 show the PDOS and d-band center for all candidate surfaces with HOCO* and CO*, respectively. Their corresponding linear fits between H concentrations and d-band centers and between adsorbate binding energies and d-band centers for all surfaces with adsorbates are shown in Figure S20 and Figure S22, respectively. It can be noticed that there are still very good scaling relations between H concentration and d-band centers for surfaces with adsorbates. And their binding energies have a good linear relation with d-band centers. This can be further concluded that increased H concentration can weaken the binding energy.

4. Conclusions

In this work, the effect of H concentration on $PdH_x(111)$ surfaces on the CO_2RR and the HER has been studied using theoretical methods. Active learning cluster expansion equipped with Monte Carlo simulated annealing has been implemented to find stable $PdH_x(111)$ surface candidates. We have obtained 12 stable candidates from converged DFT convex hull, which are Pd_{64}, $Pd_{64}H_2$, $Pd_{64}H_4$, $Pd_{64}H_8$, $Pd_{64}H_{10}$, $Pd_{64}H_{13}$, $Pd_{64}H_{31}$, $Pd_{64}H_{39}$, $Pd_{64}H_{53}$, $Pd_{64}H_{62}$, $Pd_{64}H_{63}$ and $Pd_{64}H_{64}$. We have carried out a method to find adsorption sites and then calculate the binding energies automatically. Their free energies are further calculated, illustrating the $PdH_x(111)$ surfaces with low H concentration have CO* poisoning. The scaling relations between different adsorbates show there are still good linear relations, but the segregation of H may have an influence on their scaling relations. According to the activity volcano, $Pd_{64}H_{64}$, $Pd_{64}H_{63}$ and $Pd_{64}H_{39}$ corresponding H concentrations of 1, 0.97, and 0.60 respectively, show high current densities at an overpotential of 0.5 V. The $Pd_{64}H_{39}$ surface is stable when the surface is in equilibrium with H_2 gas, and the H concentration match well with the experimentally determined 60% H concentration of Pd hydride [20]. Due to the existence of the competitive reactions between CO_2RR and HER, the selectivity plot toward CO and H_2 is calculated and illustrates these three candidates have better CO production compared to others, especially for $Pd_{64}H_{64}$. The statistical distribution of Pd and H atoms in all candidates reveals that H atoms can weaken the binding energies of all adsorbates, which may provide good guidance to tune the binding energy.

Declaration of competing interest

The authors declare that they have no known competing financial interests or personal relationships that could have appeared to influence the work reported in this paper.

Data availability

The data is published in the DTU Data repository linked to reference 38.

Acknowledgments

This work was supported by the China Scholarship Council and by the Villum Foundation through the research center V-Sustain (#9455). The authors thank the Niflheim Linux supercomputer cluster at the Department of Physics at the Technical University of Denmark.

Appendix A. Supplementary data

Supplementary material related to this article can be found online at https://doi.org/10.1016/j.jcat.2023.115188.

References

[1] N.P. Gillett, M. Kirchmeier-Young, A. Ribes, H. Shiogama, G.C. Hegerl, R. Knutti, G. Gastineau, J.G. John, L. Li, L. Nazarenko, N. Rosenbloom, Ø. Seland, T. Wu, S. Yukimoto, T. Ziehn, Nature Clim. Change 11 (3) (2021) 207–212, http://dx.doi.org/10.1038/s41558-020-00965-9.

[2] S. Nitopi, E. Bertheussen, S.B. Scott, X. Liu, A.K. Engstfeld, S. Horch, B. Seger, I.E.L. Stephens, K. Chan, C. Hahn, J.K. Nørskov, T.F. Jaramillo, I. Chorkendorff, Chem. Rev. 119 (12) (2019) 7610–7672, http://dx.doi.org/10.1021/acs.chemrev.8b00705.

[3] Z. Zhang, S.-Y. Pan, H. Li, J. Cai, A.G. Olabi, E.J. Anthony, V. Manovic, Renew. Sustain. Energy Rev. 125 (2020) 109799, http://dx.doi.org/10.1016/j.rser.2020.109799.

[4] A.R. Woldu, Z. Huang, P. Zhao, L. Hu, D. Astruc, Coord. Chem. Rev. 454 (2022) 214340, http://dx.doi.org/10.1016/j.ccr.2021.214340.

[5] S. Liang, L. Huang, Y. Gao, Q. Wang, B. Liu, Adv. Sci. 8 (24) (2021) 2102886, http://dx.doi.org/10.1002/advs.202102886.

[6] Y. Hori, R. Takahashi, Y. Yoshinami, A. Murata, J. Phys. Chem. B 101 (36) (1997) 7075–7081, http://dx.doi.org/10.1021/jp970284i.

[7] M. Ma, H.A. Hansen, M. Valenti, Z. Wang, A. Cao, M. Dong, W.A. Smith, Nano Energy 42 (2017) 51–57, http://dx.doi.org/10.1016/j.nanoen.2017.09.043.

[8] Z. Liang, L. Song, M. Sun, B. Huang, Y. Du, Sci. Adv. 7 (47) (2021) eabl4915, http://dx.doi.org/10.1126/sciadv.abl4915.

[9] T. Möller, W. Ju, A. Bagger, X. Wang, F. Luo, T.N. Thanh, A.S. Varela, J. Rossmeisl, P. Strasser, Energy Environ. Sci. 12 (2) (2019) 640–647, http://dx.doi.org/10.1039/c8ee02662a.

[10] Y. Hori, A. Murata, R. Takahashi, J. Chem. Soc., Faraday Trans. 1 85 (8) (1989) 2309, http://dx.doi.org/10.1039/f19898502309.

[11] A.A. Peterson, J.K. Nørskov, J. Phys. Chem. Lett. 3 (2) (2012) 251–258, http://dx.doi.org/10.1021/jz201461p.

[12] X. Wang, Q. Chen, Y. Zhou, H. Li, J. Fu, M. Liu, Adv. Sensor Energy Mater. 1 (3) (2022) 100023, http://dx.doi.org/10.1016/j.asems.2022.100023.

[13] F. Chang, M. Xiao, R. Miao, Y. Liu, M. Ren, Z. Jia, D. Han, Y. Yuan, Z. Bai, L. Yang, Electrochem. Energy Rev. 5 (3) (2022) 4, http://dx.doi.org/10.1007/s41918-022-00139-5.

[14] W. Zhu, R. Michalsky, Ö. Metin, H. Lv, S. Guo, C.J. Wright, X. Sun, A.A. Peterson, S. Sun, J. Am. Chem. Soc. 135 (45) (2013) 16833–16836, http://dx.doi.org/10.1021/ja409445p.

[15] Q. Lu, J. Rosen, Y. Zhou, G.S. Hutchings, Y.C. Kimmel, J.G. Chen, F. Jiao, Nature Commun. 5 (1) (2014) 3242, http://dx.doi.org/10.1038/ncomms4242.

[16] D.H. Won, H. Shin, J. Koh, J. Chung, H.S. Lee, H. Kim, S.I. Woo, Angew. Chem. Int. Ed. 55 (32) (2016) 9297–9300, http://dx.doi.org/10.1002/anie.201602888.

[17] W. Zhu, S. Kattel, F. Jiao, J.G. Chen, Adv. Energy Mater. 9 (9) (2019) 1802840, http://dx.doi.org/10.1002/aenm.201802840.

[18] W. Sheng, S. Kattel, S. Yao, B. Yan, Z. Liang, C.J. Hawxhurst, Q. Wu, J.G. Chen, Energy Environ. Sci. 10 (5) (2017) 1180–1185, http://dx.doi.org/10.1039/c7ee00071e.

[19] D. Gao, H. Zhou, F. Cai, D. Wang, Y. Hu, B. Jiang, W.-B. Cai, X. Chen, R. Si, F. Yang, S. Miao, J. Wang, G. Wang, X. Bao, Nano Res. 10 (6) (2017) 2181–2191, http://dx.doi.org/10.1007/s12274-017-1514-6.

[20] J.S. Diercks, J. Herranz, M. Georgi, N. Diklić, P. Chauhan, K. Ebner, A.H. Clark, M. Nachtegaal, A. Eychmüller, T.J. Schmidt, ACS Catalysis 12 (17) (2022) 10727–10741, http://dx.doi.org/10.1021/acscatal.2c02660.

[21] M. Johansson, E. Skúlason, G. Nielsen, S. Murphy, R. Nielsen, I. Chorkendorff, Surf. Sci. 604 (7–8) (2010) 718–729, http://dx.doi.org/10.1016/j.susc.2010.01.023.

[22] J.M. Rahm, J. Löfgren, E. Fransson, P. Erhart, Acta Mater. 211 (2021) 116893, http://dx.doi.org/10.1016/j.actamat.2021.116893.

[23] A.H. Larsen, J.J. Mortensen, J. Blomqvist, I.E. Castelli, R. Christensen, M. Dułak, J. Friis, M.N. Groves, B. Hammer, C. Hargus, E.D. Hermes, P.C. Jennings, P.B. Jensen, J. Kermode, J.R. Kitchin, E.L. Kolsbjerg, J. Kubal, K. Kaasbjerg, S. Lysgaard, J.B. Maronsson, T. Maxson, T. Olsen, L. Pastewka, A. Peterson, C. Rostgaard, J. Schiøtz, O. Schütt, M. Strange, K.S. Thygesen, T. Vegge, L. Vilhelmsen, M. Walter, Z. Zeng, K.W. Jacobsen, J. Phys.: Condens. Matter 29 (27) (2017) 273002, http://dx.doi.org/10.1088/1361-648x/aa680e.

[24] S. Bahn, K. Jacobsen, Comput. Sci. Eng. 4 (3) (2002) 56–66, http://dx.doi.org/10.1109/5992.998641.

[25] G. Kresse, J. Hafner, Phys. Rev. B 47 (1) (1993) 558–561, http://dx.doi.org/10.1103/physrevb.47.558.

[26] G. Kresse, J. Hafner, Phys. Rev. B 49 (20) (1994) 14251–14269, http://dx.doi.org/10.1103/physrevb.49.14251.

[27] P.E. Blöchl, Phys. Rev. B 50 (24) (1994) 17953–17979, http://dx.doi.org/10.1103/physrevb.50.17953.

[28] J. Wellendorff, K.T. Lundgaard, A. Møgelhøj, V. Petzold, D.D. Landis, J.K. Nørskov, T. Bligaard, K.W. Jacobsen, Phys. Rev. B 85 (23) (2012) http://dx.doi.org/10.1103/physrevb.85.235149.
[29] H.J. Monkhorst, J.D. Pack, Phys. Rev. B 13 (12) (1976) 5188–5192, http://dx.doi.org/10.1103/physrevb.13.5188.
[30] J.H. Chang, D. Kleiven, M. Melander, J. Akola, J.M. Garcia-Lastra, T. Vegge, J. Phys.: Condens. Matter 31 (32) (2019) 325901, http://dx.doi.org/10.1088/1361-648x/ab1bbc.
[31] D. De Fontaine, Solid State Physics, Elsevier, 1994, pp. 33–176, http://dx.doi.org/10.1016/s0081-1947(08)60639-6.
[32] H.A. Hansen, J.B. Varley, A.A. Peterson, J.K.N. rskov, J. Phys. Chem. Lett. 4 (3) (2013) 388–392, http://dx.doi.org/10.1021/jz3021155.
[33] J.K. Nørskov, T. Bligaard, A. Logadottir, J.R. Kitchin, J.G. Chen, S. Pandelov, U. Stimming, J. Electrochem. Soc. 152 (3) (2005) J23, http://dx.doi.org/10.1149/1.1856988.
[34] C. Ai, T. Vegge, H.A. Hansen, ChemSusChem 15 (10) (2022) 202200008, http://dx.doi.org/10.1002/cssc.202200008.
[35] A.A. Peterson, F. Abild-Pedersen, F. Studt, J. Rossmeisl, J.K. Nørskov, Energy Environ. Sci. 3 (9) (2010) 1311, http://dx.doi.org/10.1039/c0ee00071j.
[36] N. Fukumuro, Y. Fukai, H. Sugimoto, Y. Ishii, H. Saitoh, S. Yae, J. Alloys Compd. 825 (2020) 153830, http://dx.doi.org/10.1016/j.jallcom.2020.153830.
[37] J. Ye, J. Phys. Chem. C 126 (12) (2022) 5513–5520, http://dx.doi.org/10.1021/acs.jpcc.1c10064.
[38] C. Ai, J.H. Chang, A.S. Tygesen, T. Vegge, H.A. Hansen, Active learning cluster expansion studies of PdHx on CO_2 reduction, 2023, http://dx.doi.org/10.11583/DTU.21325017.
[39] B. Hammer, J. Nørskov, Theoretical Surface Science and Catalysis—Calculations and Concepts, Elsevier, 2000, http://dx.doi.org/10.1016/s0360-0564(02)45013-4.